J. Fluid Mech. (2014), *vol.* 761, *pp.* 443–463.
doi:10.1017/jfm.2014.628

Spontaneous generation of a swirling plume in a stratified ambient

Francisco Marques[1] **and Juan M. Lopez**[2,†]

[1]Departament de Física Aplicada, Universitat Politècnica de Catalunya, Barcelona 08034, Spain

[2]School of Mathematical and Statistical Sciences, Arizona State University, Tempe, AZ 85287, USA

(Received 6 August 2014; revised 6 October 2014; accepted 24 October 2014)

The transition from laminar to complex spatio-temporal dynamics of plumes due to a localized buoyancy source is studied numerically. Several experiments have reported that this transition is sensitive to external perturbations. Therefore, a well-controlled set-up has been chosen for our numerical study, consisting of a localized heat source at the bottom of an enclosed cylinder whose sidewall is maintained at a fixed temperature which varies linearly up the wall. Restricting the dynamics to the axisymmetric subspace, the first instability is to a puffing state. However, for smaller Grashof numbers, the plume becomes unstable to three-dimensional perturbations and a swirling plume spontaneously appears. The next bifurcation, viewed in the rotating frame where the plume is stationary, also exhibits puffing and suggests a connection between the unstable axisymmetric puffing solution and the swirling plume. Further bifurcations result in quasi-periodic states with a very low-frequency modulation, and these eventually become spatio-temporally complex.

Key words: nonlinear instability, plumes/thermals, stratified flows

1. Introduction

Plumes with swirl are of much interest due to their natural occurrence, such as hydrothermal plumes which rise through a weakly stratified ocean until they reach their level of neutral buoyancy (Speer & Marshall 1995; Woods 2010), as well as dust devils and fire whirls. Modelling of such plumes dates back to the seminal work of Morton, Taylor & Turner (1956), who developed a simple model by making a few assumptions, namely that the plume is fully turbulent and that its long-time average is self-similar in the vertical and axisymmetric. The model provides much insight into turbulent plumes and allows one to infer, for example, the strength of the buoyancy source based on observations of the plume's height and an estimate of the buoyancy frequency characterizing the stratified ambient. However, the simple model is not able to account for the swirl component observed in some plumes. The scales of these plumes are generally too small for the Coriolis force to be directly responsible for their swirl (Morton 1966; Carroll & Ryan 1970), and there has been a long discussion concerning the source of their vertical vorticity (Maxworthy 1973; Snow 1987; Battaglia, Rehm & Baum 2000; Fiedler & Kanak 2001). While it is generally accepted that background vorticity in the boundary layer can be concentrated and turned into the vertical direction by the localized buoyancy source initiating the

† Email address for correspondence: juan.m.lopez@asu.edu

plume, it is not clear that this is either a necessary nor unique mechanism. When the buoyancy source is uniformly distributed, such as in Rayleigh–Bénard convection, thermal plumes with a strong vertical component of vorticity have been observed in numerical simulations with no imposed mean flow and, therefore, under zero mean shear conditions (Cortese & Balachandar 1993). This is in contrast to the widely held view that the source of swirl is the interaction between buoyancy-induced vertical flow and shear associated with a mean horizontal flow. Also, in studies based on reduced equation models of Rayleigh–Bénard convection, again with zero mean shear, decomposed into toroidal and meridional components, it was found that vertical vorticity naturally arises from symmetry breaking (Murphy & Lopez 1984; Massaguer & Mercader 1988; Massaguer, Mercader & Net 1990).

While most laboratory experiments simulating these natural plumes use imposed swirl, such as rotating outer screens (Emmons & Ying 1967; Muraszew, Fedele & Kuby 1979; Snow 1987), there is also at least one experiment that we are aware of where a swirling plume was observed in a stationary enclosure (Torrance 1979). That study was experimental, using flow visualization together with axisymmetric numerical simulations. In certain parameter regimes, where the background stratification was not too large and not too small, non-axisymmetric disturbances were observed once the Grashof number, parameterizing the localized heat source, exceeded a critical value. Unfortunately, the details concerning the swirling plume state were very limited. The swirling states that were observed experimentally were not reproduced by the axisymmetric simulations and the origin of the swirl and non-axisymmetric nature of the experimentally observed flow remained unexplained. These open questions motivate the present study. We have used a similar geometry, consisting of a completely enclosed circular cylinder with prescribed temperature on all walls (details are given in the following section), and have indeed found a regime in which swirl is spontaneously generated as a result of symmetry breaking. The subsequent bifurcations for moderate Grashof numbers are also analysed, and comparisons are made with a similar enclosed problem but without the imposed background stratification (Torrance, Orloff & Rockett 1969; Torrance & Rockett 1969; Lopez & Marques 2013). In order to characterize the bifurcations from the steady basic state to complex spatio-temporal behaviour, dynamical systems theory has been used (Strogatz 1994; Kuznetsov 2004), and in particular bifurcations with symmetry, which are relevant to many fluid problems (Crawford & Knobloch 1991; Chossat & Lauterbach 2000).

2. Governing equations and numerical technique

Consider the flow in a circular cylinder of radius R and length L, with no-slip boundary conditions, and with an imposed temperature profile at the cylinder wall. The bottom endwall has a fixed temperature T_0^* except for a disk of diameter D at the bottom centre with a hotter temperature T_h^*. The top endwall is kept at a temperature T_t^*, and the temperature varies linearly along the sidewall between T_0^* at the bottom and T_t^* at the top, resulting in a stable stratification, but for the hot spot at the bottom. There are horizontal and vertical temperature gradients, driven by the differences $T_h^* - T_0^*$ and $T_t^* - T_0^*$ respectively. Figure 1(*a*) shows a schematic of the cylinder. The boundary conditions for the temperature (not considering the hot disk) result in a stable stratification $\rho(z^*) = \rho_0(1 - \alpha(T^*(z^*) - T_0^*)) = \rho_0(1 - \alpha(T_t^* - T_0^*)z^*/L)$, and the corresponding Brunt–Väisälä frequency N_{BV} is

$$N_{BV}^2 = -(g/\rho_0)\mathrm{d}\rho(z^*)/\mathrm{d}z^* = \rho_0\alpha(T_t^* - T_0^*)/L, \tag{2.1}$$

where α is the coefficient of thermal expansion and ρ_0 is the density at temperature T_0^*.

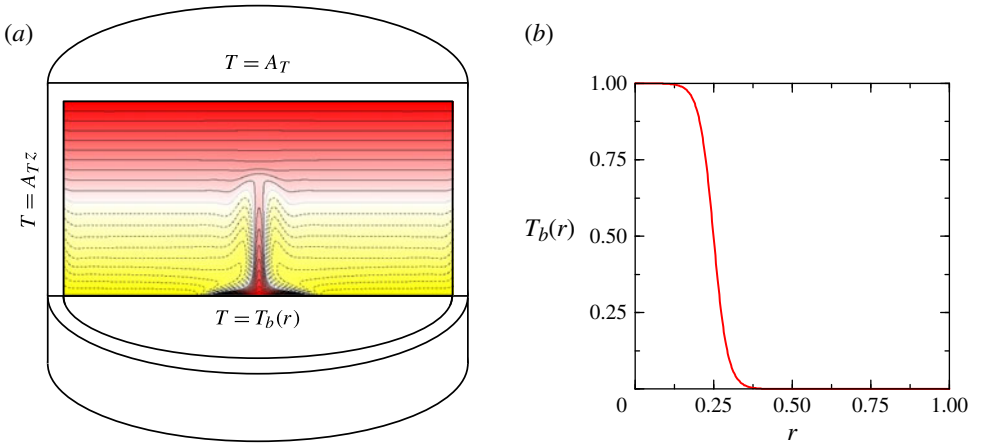

FIGURE 1. (Colour online) (*a*) Schematic of the apparatus with contours of non-dimensional temperature T showing a laminar thermal plume emerging from the localized heating at the base centre for $Gr = 10^5$, $\sigma = 7$, $A_r = A_z = 2$ and $A_T = 1$. (*b*) Radial temperature profile at the bottom wall (2.7) along a diameter, for the same geometry as (*a*), $C = 7.4$ and $\epsilon = 1/3$.

The Boussinesq approximation is implemented, treating all fluid properties as constant except for a linear variation of density with temperature in the gravitational buoyancy term. The system is non-dimensionalized using L as the length scale, L^2/κ as the time scale (κ is the thermal diffusivity), $T_h^* - T_0^*$ as the temperature scale, and $\kappa^2\rho_0/L^2$ as the pressure scale. The non-dimensional governing equations are

$$(\partial_t + \boldsymbol{u}\cdot\boldsymbol{\nabla})\boldsymbol{u} = -\boldsymbol{\nabla}p + \sigma\nabla^2\boldsymbol{u} + N^2\,T\boldsymbol{e}_z, \tag{2.2}$$

$$(\partial_t + \boldsymbol{u}\cdot\boldsymbol{\nabla})T = \nabla^2 T, \qquad \boldsymbol{\nabla}\cdot\boldsymbol{u} = 0, \tag{2.3}$$

where $\boldsymbol{u} = (u, v, w)$ is the velocity in cylindrical coordinates $(r, \theta, z) \in [0, A_r/A_z] \times [0, 2\pi] \times [0, 1] = \mathscr{D}$, the corresponding vorticity is $\boldsymbol{\omega} = \boldsymbol{\nabla}\times\boldsymbol{u} = (\xi, \eta, \zeta)$, p is the dynamic pressure, $\boldsymbol{e}_z = (0, 0, 1)$ is the vertical unit vector in the z-direction and $T = (T^* - T_0^*)/(T_h^* - T_0^*)$ is the non-dimensional temperature, while T^* is the dimensional temperature. N is the non-dimensional Brunt–Väisälä frequency $N = N_{BV}L^2/\kappa$. The non-dimensional parameters are

$$\left.\begin{array}{ll} \text{Grashof number} & Gr = \alpha g D^3(T_h^* - T_0^*)/\nu^2, \\ \text{Prandtl number} & \sigma = \nu/\kappa, \\ \text{cylinder to hot spot radial ratio} & A_r = R/D, \\ \text{axial aspect ratio} & A_z = L/D, \\ \text{temperature ratio} & A_T = (T_t^* - T_0^*)/(T_h^* - T_0^*), \end{array}\right\} \tag{2.4}$$

where ν is the kinematic viscosity and g is the acceleration due to gravity. We have introduced a Grashof number based on the hot-spot diameter D, as is typically done in natural convection problems due to localized heating (Torrance 1979), rather than a dimension of the container. The relationship between the Grashof number and the non-dimensional Brunt–Väisälä frequency is

$$N^2 = \sigma^2 A_T A_z^3 Gr. \tag{2.5}$$

The boundary conditions are:

$$\left.\begin{array}{lll} r = A_r/A_z\text{:} & T = A_T z, & u = v = w = 0, \\ z = 1\text{:} & T = A_T, & u = v = w = 0, \\ z = 0\text{:} & T = T_b(r), & u = v = w = 0. \end{array}\right\} \tag{2.6}$$

The temperature profile at the bottom wall has been regularized so that instead of a step function, it is of the form

$$T_b(r) = \frac{1}{1 + \exp\left(\dfrac{C}{\epsilon}\left(A_z r - \dfrac{1}{2}\right)\right)}, \quad r \in [0, A_r/A_z], \tag{2.7}$$

where $1/(2A_z) = D/(2L)$ is the non-dimensional radius of the hot disk, and ϵ is the non-dimensional length where most of the temperature variation takes place. We have taken $C = 7.4$ so that 95 % of the temperature variation takes place in an interval of length ϵ centred at the hot-disk radius, $r \in [(1-\epsilon)/(2A_z), (1+\epsilon)/(2A_z)]$. Figure 1(*b*) shows the radial temperature profile imposed at the bottom wall, for $\epsilon = 1/3$, which is the value used for the simulations. In practice it is impossible to maintain a sharp temperature jump, so the regularization (2.7) mimics the real physical situation, and also helps to improve the convergence of the spectral method used in the numerical simulations.

The main parameter that controls the validity of the Boussinesq approximation is $\alpha(T_t^* - T_0^*)$, which is independent of the other governing parameters; validity requires $\alpha(T_t^* - T_0^*) \ll 1$ (Busse 1967; Gray & Giorgini 1976). For the Grashof numbers considered in this study, $Gr \leqslant 3.5 \times 10^5$, this requirement is easily satisfied with typical laboratory-scale experiments. For example, using water and $D = 3$ cm (corresponding to a cylinder of radius and height of 6 cm), and $T_t^* - T_0^* < 8\,^\circ$C, $Gr \sim 4.5 \times 10^5$ can be achieved while $\alpha(T_t^* - T_0^*) < 2 \times 10^{-3} \ll 1$. For air, using $D = 12$ cm (corresponding to a cylinder of radius and height of 24 cm), and $T_t^* - T_0^* < 2\,^\circ$C, $Gr \sim 5 \times 10^5$ can be achieved while $\alpha(T_t^* - T_0^*) < 7 \times 10^{-3} \ll 1$. Of course, using a larger apparatus and/or different fluids, there is ample room for reaching even larger Grashof numbers while maintaining the validity of the Boussinesq approximation.

The governing equations have been solved using a second-order time-splitting method, with space discretized via a Galerkin–Fourier expansion in θ and Chebyshev collocation in r and z. The spectral solver is based on that described by Mercader, Batiste & Alonso (2010) and it has recently been used in our previous study of plumes in an isothermal (non-stratified) ambient (Lopez & Marques 2013). For the solutions presented here, with $A_r = A_z = 2$ and $A_T = 1$, we have used up to $n_r = 256$ and $n_z = 128$ Chebyshev modes in the radial and axial directions and $n_\theta = 36$ azimuthal Fourier modes. The number of Chebyshev spectral modes is high in order to well-resolve the plume structure and the rapid variation of the temperature and the boundary layer forming at the bottom wall. The solution is well-resolved with at least four orders of magnitude of decay in the modal energies.

The L_2-norms of the azimuthal Fourier modes of a given solution,

$$E_m = \frac{1}{2}\int_{z=0}^{z=1}\int_{r=0}^{r=\gamma} \boldsymbol{u}_m \cdot \boldsymbol{u}_m^* \, r \, \mathrm{d}r \, \mathrm{d}z, \tag{2.8}$$

where $\boldsymbol{u}_m$ is the mth Fourier mode of the velocity field and $\boldsymbol{u}_m^*$ is its complex conjugate, provide a convenient way to characterize the non-axisymmetric states. For axisymmetric states, E_0 is the non-dimensional kinetic energy of the flow.

The governing equations and boundary conditions are invariant under arbitrary rotations around the cylinder axis and reflections about meridional planes. These symmetries (orthogonal transformations) act simultaneously on the points in the fluid domain and also on vector fields. If $\boldsymbol{S}$ is the matrix of one of these symmetry transformations, its action $\tau(\boldsymbol{S})$ on the velocity field $\boldsymbol{u}(\boldsymbol{r})$ is given by $\tau(\boldsymbol{S})\boldsymbol{u}(\boldsymbol{r}) = \boldsymbol{S}\boldsymbol{u}(\boldsymbol{S}^{-1}\boldsymbol{r})$ (see Chossat & Lauterbach 2000, § 1.2.4), or equivalently $\tau(\boldsymbol{S})\boldsymbol{u}(\boldsymbol{S}\boldsymbol{r}) = \boldsymbol{S}\boldsymbol{u}(\boldsymbol{r})$. These equations say that in order to obtain the symmetrically related velocity field, $\tau(\boldsymbol{S})\boldsymbol{u}$, of a given field $\boldsymbol{u}$, one takes the velocity vector at a point $\boldsymbol{r}$, transforms it according to $\boldsymbol{S}$, and translates the result to the transformed point $\boldsymbol{S}\boldsymbol{r}$. Using cylindrical coordinates and the cylindrical components of the velocity field, the action of the two symmetries in our problem is given by

$$\tau(R_\alpha)(u, v, w)(r, \theta, z, t) = (u, v, w)(r, \theta - \alpha, z, t), \tag{2.9a}$$

$$\tau(K_\beta)(u, v, w)(r, \theta, z, t) = (u, -v, w)(r, 2\beta - \theta, z, t), \tag{2.9b}$$

where α and β are arbitrary angles, R_α is the rotation of angle α about the cylinder axis, and K_β is the reflection about the meridional plane $\theta = \beta$. R_α and K_β do not commute ($K_\beta R_\alpha = R_{-\alpha} K_\beta$), and generate the group $O(2)$ (orthogonal matrices in two dimensions) acting on the periodic azimuthal θ-direction. The action of these symmetries on the vorticity is given by

$$\tau(R_\alpha)(\xi, \eta, \zeta)(r, \theta, z, t) = (\xi, \eta, \zeta)(r, \theta - \alpha, z, t), \tag{2.10a}$$

$$\tau(K_\beta)(\xi, \eta, \zeta)(r, \theta, z, t) = (-\xi, \eta, -\zeta)(r, 2\beta - \theta, z, t). \tag{2.10b}$$

A vector field is $\boldsymbol{S}$-symmetric, or equivariant under $\boldsymbol{S}$, if $\tau(\boldsymbol{S})\boldsymbol{u}(\boldsymbol{r}) = \boldsymbol{u}(\boldsymbol{r})$, i.e. it coincides with the $\boldsymbol{S}$-transformed field; an equivalent expression is $\boldsymbol{S}\boldsymbol{u}(\boldsymbol{r}) = \boldsymbol{u}(\boldsymbol{S}\boldsymbol{r})$. As a consequence, the basic steady flow, which possesses all the symmetries of the problem, is axisymmetric (independent of θ), and also equivariant under meridional reflections K_β. A field that is equivariant under K_β is said to be parity symmetric.

Another useful quantity is the helicity He of a given solution, defined as the integral over the fluid domain $\mathscr{D}$ of the scalar product of the velocity and vorticity fields:

$$He = \int_{\mathscr{D}} \boldsymbol{u} \cdot \boldsymbol{\omega} \, \mathrm{d}V. \tag{2.11}$$

The local helicity $\boldsymbol{u} \cdot \boldsymbol{\omega}$ is invariant under rotations R_α, but is not invariant under parity (the action of K_β):

$$\tau(K_\beta)\boldsymbol{u} \cdot \boldsymbol{\omega}(r, \theta, z, t) = -\boldsymbol{u} \cdot \boldsymbol{\omega}(r, 2\beta - \theta, z, t). \tag{2.12}$$

An important consequence is that parity-symmetric solutions (invariant under K_β) have zero helicity, and therefore He is a good measure of the parity breaking processes that are related to the spontaneous generation of swirl.

3. Basic state

For moderate values of the Grashof number, Gr, the solution of the governing equations is a steady and axisymmetric basic state, BS. For the results presented here, we have fixed all the other parameters at $A_r = 2, A_z = 2, A_T = 1$ and $\sigma = 7$, and have varied Gr over several decades. The choice of $A_T = 1$ means that the centre of the hot spot on the bottom is at the same temperature as the top endwall, and so the

neutral buoyancy level of a well-developed plume will be roughly halfway between the top and bottom. Keeping A_T fixed means that the strength of the stratification is then proportional to Gr, and this is reflected in the buoyancy frequency squared being proportional to Gr. The Prandtl number $\sigma = 7$ nominally corresponds to water as the working fluid. The solutions are quantitatively dependent on the geometric parameters A_r and A_z but, for reasonable variations, the results are qualitatively independent of these.

The localized heating in the centre of the bottom endwall means that there is a non-zero radial temperature gradient for any non-zero Gr. This radial temperature gradient locally produces azimuthal vorticity resulting in a meridional circulation drawing fluid radially inward above the heated portion of the lower endwall and upward along the axis, eventually forming a thermal plume for larger Gr. The vertical extent of this axial plume is limited by the vertical stratification, and the diffusion of both temperature and vorticity.

Figure 2 shows the structure of the base state in terms of isotherms and streamlines at $Gr = 10$, 10^3 and 10^5. In this range of Gr, the base state is stable and there are substantial changes in the flow structure. The streamlines are isolevels of the streamfunction ψ, where the meridional velocity components are $(u, w) = (-\partial\psi/\partial z, \partial\psi/\partial r)/r$. For $Gr = 10^2$ and smaller, the flow is conduction dominated; the velocity is very small, as can be observed from the values of the streamfunction and the spacing between the streamlines, and the hot-spot temperature diffuses throughout the whole domain. For larger Grashof numbers ($Gr \sim 10^3$) the velocity intensifies above the hot spot and a thermal plume begins to form. As the plume fluid rises, its temperature dissipates, and when the temperature of the rising fluid matches the ambient temperature, it stops rising and spreads out radially, creating a large-scale circulation in the bottom half of the container (up to the neutral buoyancy level), while in the upper part of the container the fluid is essentially stagnant and linearly stratified.

By $Gr = 10^5$, a well-developed plume has formed (see figure 2*e,f*). The temperature in the plume still drops as the fluid rises, as in the lower-Gr cases, but now as the plume fluid reaches the neutral buoyancy level it retains upward momentum resulting in an overshoot beyond the neutral buoyancy level before it stagnates vertically, falls back to the neutral level and continues to flow out radially. In the upper part, the flow is essentially stagnant and linearly stratified, matching the imposed linear temperature profile imposed on the sidewall. In the lower part, the return flow of the plume generates a meridional circulation. The meridional circulation generates a thermal boundary layer at the sidewall, and between this boundary layer and the plume, the temperature is essentially linearly stratified, but with a slightly different stratification from the imposed linear profile at the sidewall.

Figure 3 shows vertical profiles at the axis of the temperature $T(r = 0, z)$ and the vertical velocity $w(r = 0, z)$. We have used these profiles for a quantitative measurement of the plume height, z_{PH}, defined as the stagnation point of the plume where $w(r = 0, z_{PH}) = 0$, and the neutral buoyancy level z_{NB}, defined as the height at which the plume temperature (and density) equals the ambient temperature. The long-dashed lines in figure 3 are the T- and w-profiles at mid-radius ($r = 0.5A_r$). Figure 4 shows the variations in z_{PH} and z_{NB} over a range of Gr for which the base state is stable. For small $Gr \lesssim 10^3$, the plume is not well-developed and so the plume height is ill-defined (see figure 3*a,d* where there is a global meridional circulation driven by the hot spot, but the flow does not stagnate on the axis except at the top and bottom endwalls). The neutral buoyancy level is lower than the top endwall

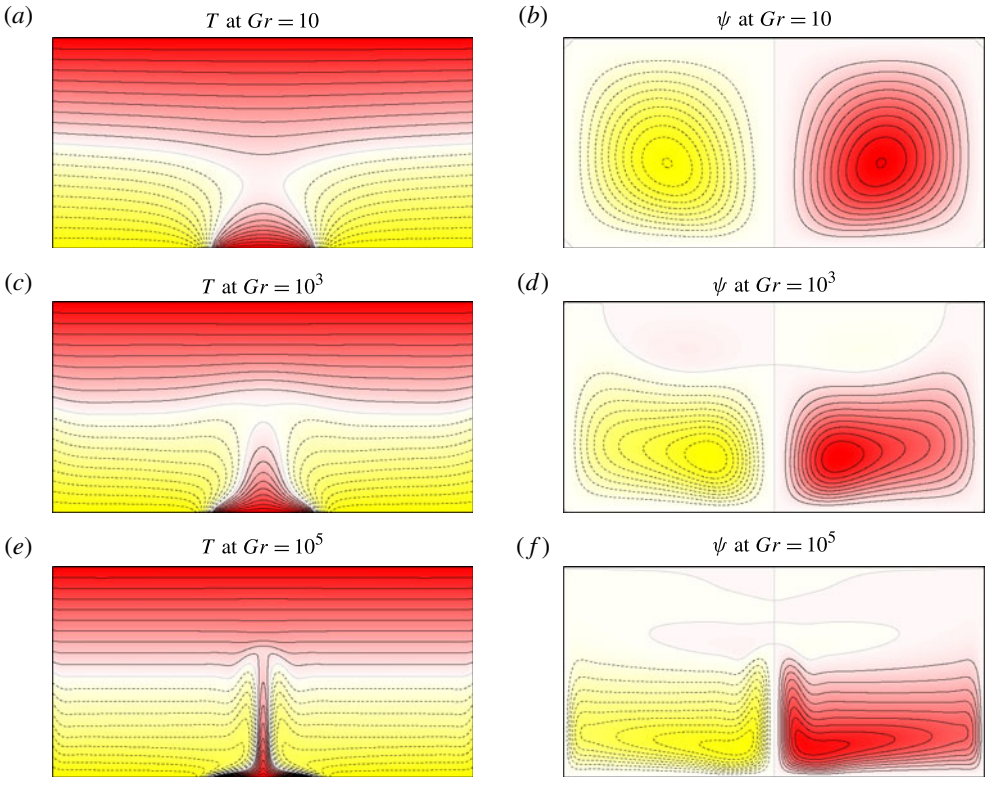

FIGURE 2. (Colour online) Isotherms (*a,c,e*) and streamlines (*b,d,f*) of the steady axisymmetric basic state BS at $A_r = 2$, $A_z = 2$, $A_T = 1$, $\sigma = 7$ and Gr as indicated. There are 10 contour levels with $T \in [-0.5, 0.5]$, and $\psi \in [-0.042, 0.042]$ for $Gr = 10$, $\psi \in [-0.92, 0.92]$ for $Gr = 10^3$, and $\psi \in [-3.5, 3.5]$ for $Gr = 10^5$; solid lines (red) are positive and dashed lines (yellow) are negative.

for $Gr > 10$ and decreases with increasing Gr for small Gr until the flow begins to undergo the transition from being conduction dominated to convection dominated and the plume begins to be well-established, at approximately $Gr = 300$. With further increases in Gr, the neutral buoyancy level grows monotonically with Gr. The plume height is always larger than the neutral buoyancy level; it decreases with increasing Gr until $Gr \approx 2 \times 10^4$, suggesting that the transition regime from conduction- to convection-dominated flow is broadly between $Gr = 300$ and $Gr = 2 \times 10^4$. The weaker stratification below the neutral buoyancy height, mentioned earlier, is clearly seen in figure 3(*c*) by comparing the vertical temperature profile in the ambient (at mid-radius, drawn as a dashed grey curve, red online) to the imposed linear temperature profile at the sidewall (drawn as a solid grey line).

4. Axisymmetric puffing plume

By increasing the Grashof number above 10^5 and keeping the simulations axisymmetric, the basic state ceases to be stable, and a periodic solution appears. In terms of dynamical systems theory, we say that the basic state undergoes a Hopf bifurcation. The instability is due to the development of a buoyancy anomaly

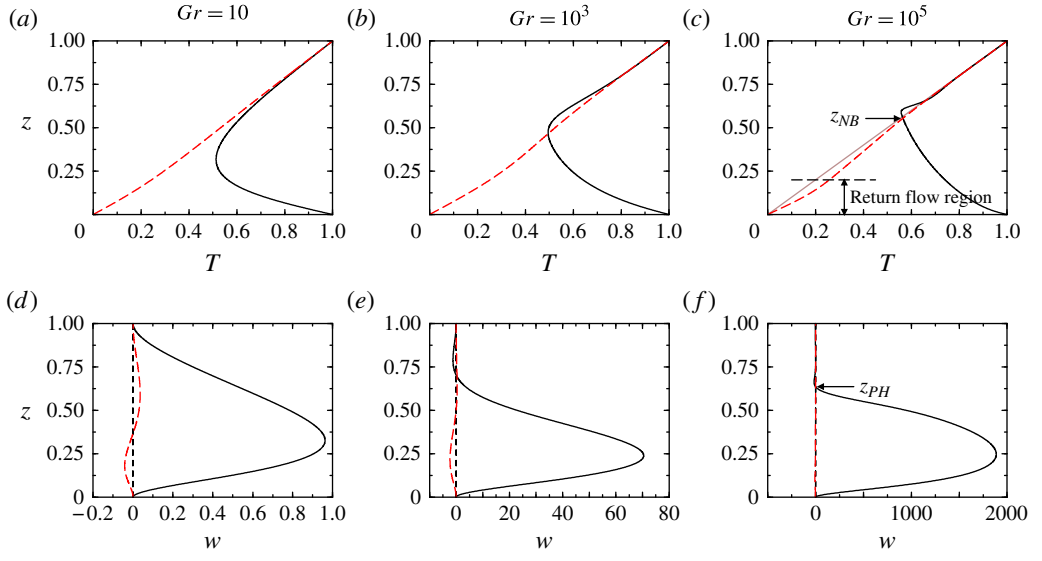

FIGURE 3. (Colour online) Profiles of temperature $T(z)$ and vertical velocity $w(z)$ of the steady axisymmetric basic state BS at $A_r = 2$, $A_z = 2$, $A_T = 1$ and $\sigma = 7$, for Gr as indicted. The solid black lines are the profiles at the plume centre, $r = 0$. The dashed grey (red online) lines are the profiles at mid-radius $r = 0.5A_r$. The grey line in (*c*) is the imposed temperature profile at the sidewall, $r = A_r$, and the vertical short-dashed line at $w = 0$ in (*d–f*) is the vertical axis to help assess the rising or descending flow in the ambient.

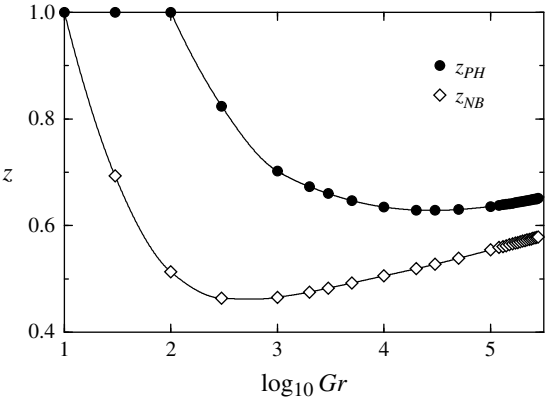

FIGURE 4. Variation of the plume height, z_{PH}, and neutral buoyancy level, z_{NB}, with Gr for $A_r = 2$, $A_z = 2$, $A_T = 1$ and $\sigma = 7$.

near the hot spot; this develops into a localized blob of fluid which rises faster than the fluid in the plume in the underlying unstable steady solution. This limit-cycle mode from an axisymmetric instability is very much the same as in the non-stratified ambient localized heating problem (Lopez & Marques 2013), the so-called puffing plume. The onset of the puffing plume, for the parameters considered here, is at $Gr \approx 2.84 \times 10^5$. Figure 5 shows four snapshots over one puffing period at $Gr = 3.5 \times 10^5$; the supplementary movies 1 and 2 available online

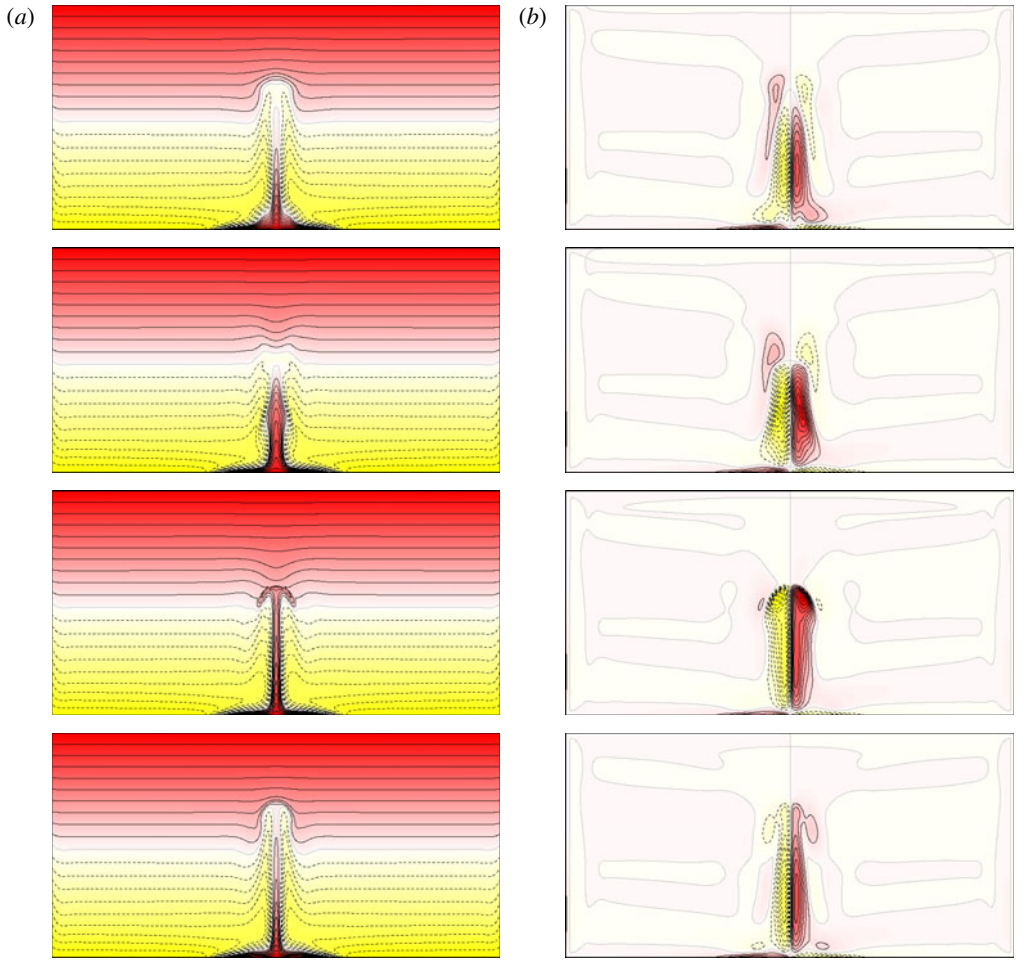

FIGURE 5. (Colour online) Isotherms (*a*) and azimuthal vorticity contours (*b*) of the axisymmetric periodic puffing plume state at $Gr = 3.5 \times 10^5$, $A_r = 2$, $A_z = 2$, $A_T = 1$ and $\sigma = 7$ at four equispaced phases over one puffing period $2\pi/\omega_0 \approx 3.9 \times 10^4$; there are 20 contour levels with $T \in [-0.5, 0.5]$ and $\eta \in [-10^5, 10^5]$; solid lines (red) are positive and dashed lines (yellow) are negative. See associated online movies 1 and 2.

at http://dx.doi.org/10.1017/jfm.2014.628 clearly shows the development of the puffs. For a range of Gr following the Hopf bifurcation, the puffing frequency, ω_0, grows monotonically with Gr, as does the buoyancy frequency N ($N \sim \sqrt{Gr}$); ω_0 is larger than N ($\omega_0 \sim 1.4N$), and so the puffing plume does not drive internal waves. From both the online movies 1 and 2 and figure 5, it is clear that the azimuthal vorticity is localized on the hot spot and in the plume up to about the neutral buoyancy height, as are the radial temperature gradients.

At $Gr \approx 4.7 \times 10^5$, the puffing plume undergoes a period-doubling bifurcation: the blob in the plume develops into a vortex ring whose radius expands while the central plume column remains intact. At the next cycle the remains of the ring are still there, impeding the subsequent blob developing into a ring, and the blob instead travels up the central column which overshoots the neutral buoyancy level higher than in the

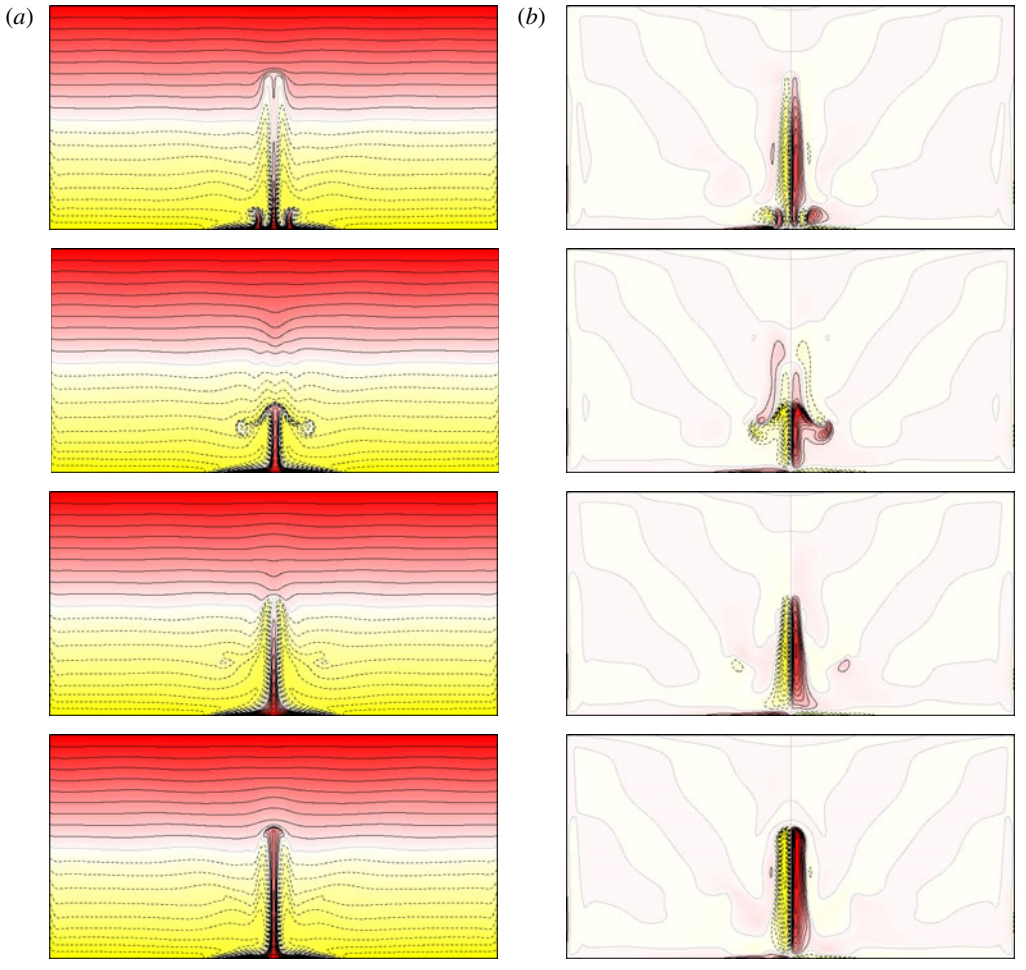

FIGURE 6. (Colour online) Isotherms (a) and azimuthal vorticity contours (b) of the axisymmetric periodic puffing plume state at $Gr = 1 \times 10^6$, $A_r = 2$, $A_z = 2$, $A_T = 1$ and $\sigma = 7$ at four phases over one period $2\pi/\omega \approx 4\pi/\omega_0 \approx 4.1 \times 10^4$; there are 20 contour levels with $T \in [-0.5, 0.5]$ and $\eta \in [-2 \times 10^5, 2 \times 10^5]$; solid lines (red) are positive and dashed lines are negative. See associated online movies 3 and 4.

previous cycle. The next cycle coincides with the previous one, resulting in a period-doubling bifurcation. Figure 6 shows four equispaced snapshots of the period-doubled puffing plume, over one period at $Gr = 1 \times 10^6$; the first two snapshots clearly show the formation of the vortex ring, which rises to about half the neutral buoyancy height. The last two snapshots, corresponding to the next puffing cycle, do not have an outer ring, and the central plume rises higher. The movies 3 and 4 available online shows further details of the period-doubled state.

Figure 7 shows time series of the global kinetic energy E_0 after transients had died down, for various values of Gr. Figure 7(a) is for a periodic puffing state at $Gr = 3.5 \times 10^5$ with (primary) frequency ω_0, where each peak corresponds to a puffing event. Figure 7(b) shows the period-doubled state at $Gr = 6 \times 10^5$. Each peak corresponds to a puffing event, but the energy of consecutive puffs is different due

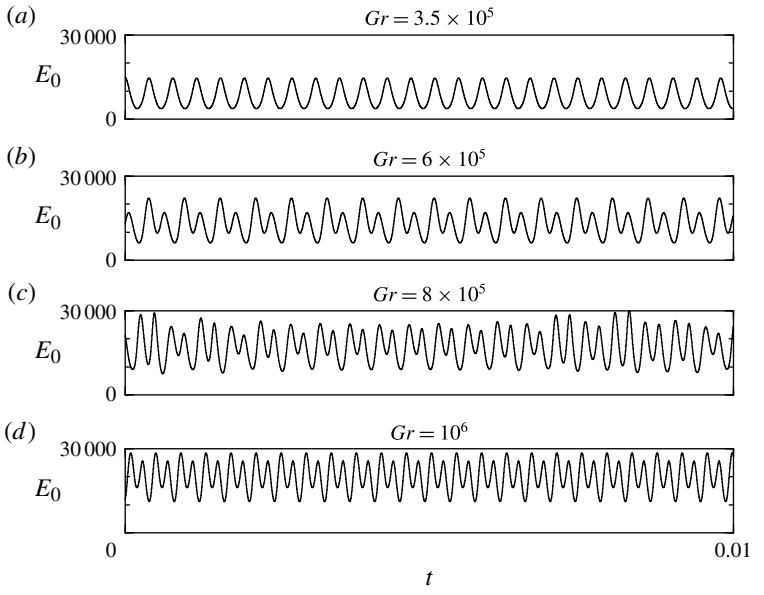

FIGURE 7. Times series of E_0 over a time interval of 0.01, taken some time after transients had died down, for various values of Gr as indicated.

to the detachment between the outer ring and the central hot column, and so the state shown is periodic, with a (primary) frequency of half the puffing frequency. In figure 7(*c*) at $Gr = 8 \times 10^5$ the frequencies associated with the central column and outer ring are not in a rational ratio, so the resultant regime is quasi-periodic. These states have a primary frequency close to $\omega_0/2$ and an additional low beating frequency. In figure 7(*d*) at $Gr = 1 \times 10^6$ they have synchronized again, and the primary frequency is $\omega_0/2$.

The period doubling results in the time-dependent flow having a frequency peak at half the puffing frequency. This new frequency peak is lower than N and internal waves result. Figure 8 shows how the frequency varies with Gr, and compares it to N. For $Gr > 4.8 \times 10^5$, the flow is quite complicated temporally, becoming quasi-periodic and then synchronizing, then quasi-periodic again, with some very long-period modulations over short intervals in Gr, suggesting that there are resonant dynamics at play. Nevertheless, there is a strong temporal signal such that the associated frequency, $\omega_0/2$, results in internal waves at approximately 40° to the vertical. This angle comes from the dispersion relation for internal waves, and is given by $\arccos(\omega_0/2N)$, although in actuality it is the local buoyancy frequency rather than that corresponding to the imposed sidewall boundary temperature profile that is relevant. From figure 3 we see that these two buoyancy frequencies are quite similar in the region above the neutral buoyancy height. This is consistent with many experimental observations of internal waves emerging from regions with localized instabilities and turbulence into a stratified region having frequencies in a narrow band about the local buoyancy frequency divided by $\sqrt{2}$ (Munroe & Sutherland 2014), and Sutherland & Linden (1998) have shown using a linear theory that internal waves within this band of frequencies are the most efficient in extracting energy from the turbulent region and transporting it through the stratified region. They also suggest that these waves feed back upon the turbulent region and modify its

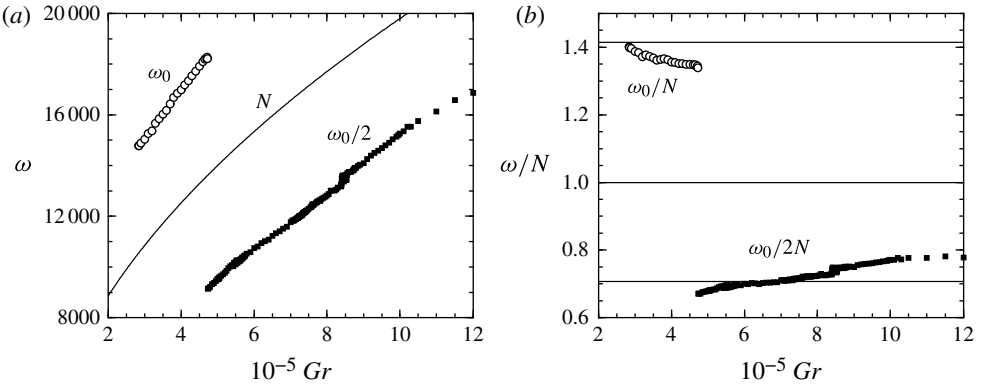

FIGURE 8. (*a*) Variation of the primary frequency of the axisymmetric puffing plumes ω versus Gr; the curve is the non-dimensional buoyancy frequency N, the open symbols correspond to limit cycle puffing states and the filled symbols are various puffing states that are generally quasi-periodic, but some have frequency locked to being periodic. The puffing frequency is ω_0. (*b*) The same results scaled by N; the three horizontal lines are at $\omega_0/N = 2/\sqrt{2}$, 1, and $1/\sqrt{2}$.

mean properties to the extent that waves in this preferred frequency band are further enhanced. Similar mechanisms seem to be in play in the puffing plume regime.

5. Spontaneous generation of swirl

The puffing plume dynamics described in the previous section were from simulations restricted to the axisymmetric subspace. When the dynamics is not restricted and general three-dimensional perturbations are allowed, the base state BS loses stability at Gr lower than that for the onset of the axisymmetric puffing mode. For the parameter values studied here, instability to three-dimensional flow occurs at $Gr \approx 1.18 \times 10^5$.

It is well-known (Crawford & Knobloch 1991; Knobloch 1996) that breaking $O(2)$ symmetry can result in either standing or rotating waves if the bifurcating eigenvalue is complex (symmetry-breaking Hopf bifurcation), and which one occurs is very much problem dependent. Moreover, due to the reflection symmetry, the rotating wave's sense of rotation can be positive or negative; both solutions bifurcate simultaneously, and which one is observed depends on the initial conditions. In our problem, the base state becomes unstable and a periodic solution in the form of a rotating wave with azimuthal wavenumber $m = 1$ appears. Figure 9 shows the modal energies E_0 and E_1 of the solutions obtained up to $Gr = 4 \times 10^5$. The rotating wave solution branch RW undergoes a number of subsequent bifurcations as Gr is increased, which are described below. We begin by describing the characteristics of the rotating wave state.

Figure 10(*a*) shows the variation of the absolute value of the precession frequency ω_{pr}, scaled by N, with Gr. It shows that $|\omega_{pr}|/N \sim 1/\sqrt{2}$, and so internal waves are excited by the rotating wave state, RW, and are emitted at approximately 45°, much like the internal waves in the period-doubled axisymmetric puffing plume. The RW state has non-trivial swirl, as measured by the helicity. Figure 10(*b*) shows how He grows from zero at the Hopf bifurcation at which RW emerges. Near onset, $|He| \sim Gr \sim N^2$, and since He is a quadratic quantity, the bifurcating velocity perturbation

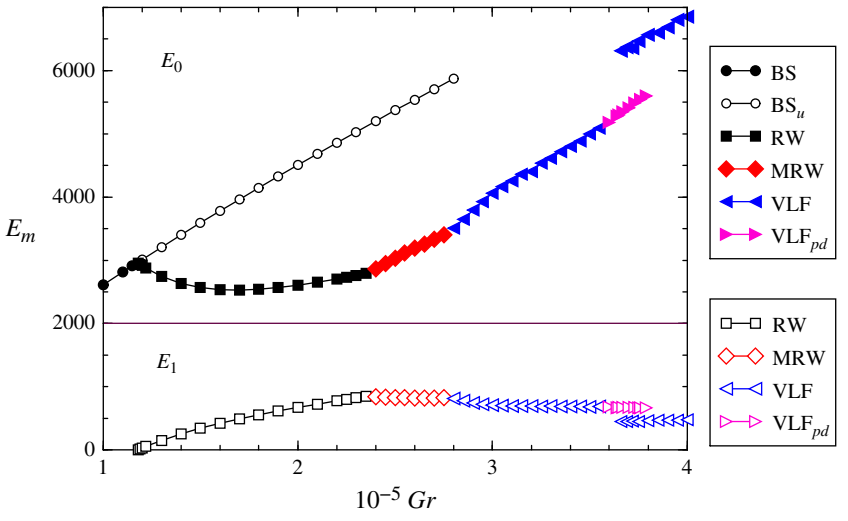

FIGURE 9. (Colour online) Variation of the modal energies (see (2.8)), E_0 and E_1, with Gr of the various states as indicated.

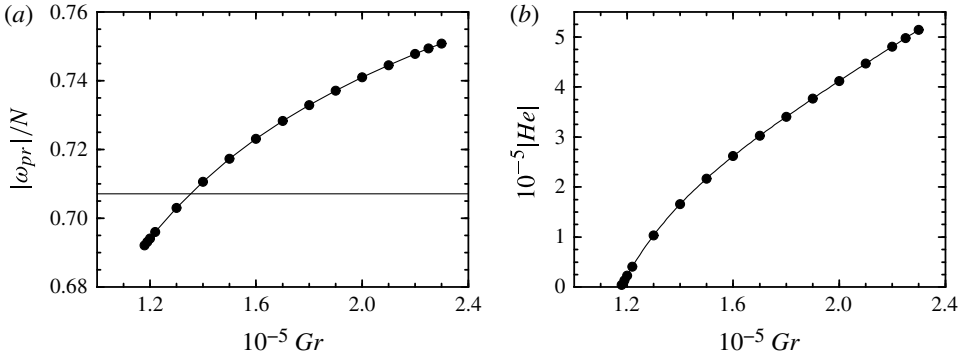

FIGURE 10. Variations of (*a*) precession frequency scaled by N and (*b*) helicity with Gr of the rotating wave state RW, showing the supercritical character of the Hopf bifurcation (absolute values are shown as RW come as conjugate pairs with opposite senses of rotation).

magnitude scales with $\sqrt{Gr} \sim N$, in agreement with the theory of a supercritical Hopf bifurcation (Kuznetsov 2004).

Figure 11 shows isotherms and contours of azimuthal vorticity in a meridional plane for the RW state at $Gr = 2 \times 10^5$. It clearly shows that the plume is tilted, and therefore the reflection symmetry is broken. As is well-known from bifurcation theory (Knobloch 1996), a Hopf bifurcation breaking axisymmetry from an $O(2)$-symmetric state may result in rotating waves when the reflection symmetry is broken, or standing waves when it is preserved. Figure 12(*a*) show isosurfaces of azimuthal vorticity η of this solution, indicating that it has azimuthal wavenumber $m = 1$, and the online movie 5 shows that it is a rotating wave: the plume does not change shape, but precesses about the vertical axis at a constant rate ω_{pr}, given in figure 10(*a*). The RW solutions come in pairs, one rotating clockwise and the other rotating

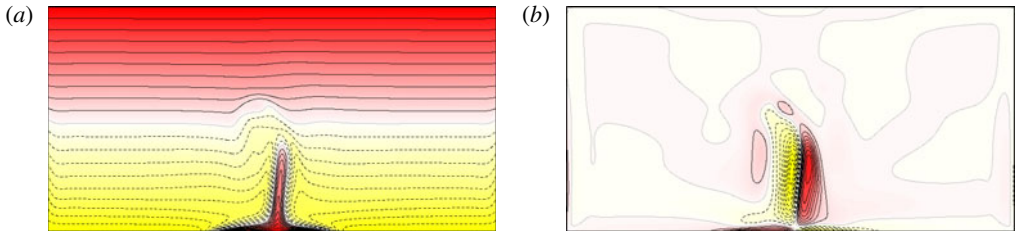

FIGURE 11. (Colour online) Snapshots of (*a*) isotherms and (*b*) azimuthal vorticity contours in a meridional plane, at an instant in time of the rotating wave state RW at $Gr = 2 \times 10^5$, $A_r = 2$, $A_z = 2$, $A_T = 1$ and $\sigma = 7$. There are 10 contour levels with $T \in [-0.5, 0.5]$ and $\eta \in [-5 \times 10^4, 5 \times 10^4]$; solid lines (red) are positive and dashed lines (yellow) are negative.

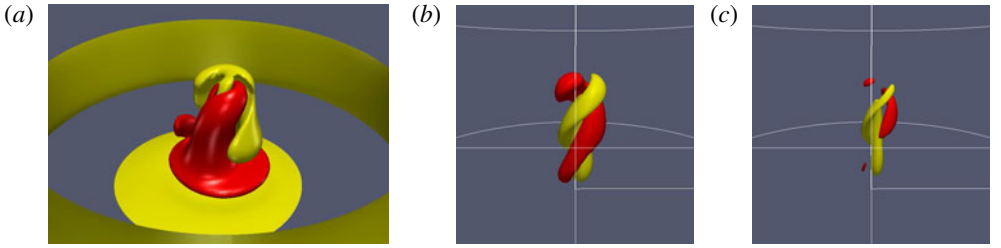

FIGURE 12. (Colour online) (*a*) Three-dimensional isosurfaces of azimuthal vorticity η, at an instant in time of the rotating wave state RW at $Gr = 2 \times 10^5, A_r = 2, A_z = 2, A_T = 1$ and $\sigma = 7$, and the isosurface levels are at $\eta = \pm 10^3$. The online movie 5 show the isosurfaces over one precession period $2\pi/\omega_{pr} \approx 5 \times 10^{-4}$. Three-dimensional isosurfaces of vertical vorticity ξ of the same state, at levels (*b*) $\xi = \pm 2000$ and (*c*) $\xi = \pm 4000$.

counter-clockwise. This symmetry-breaking process is responsible for the spontaneous generation of swirl. Figure 12(*b*) shows the structure of the plume: the isosurfaces of axial vorticity at $\xi = \pm 2000$ show that the plume consists of two intertwined vortices with opposite sense of rotation. Both vortices have positive vertical velocity, but opposite ξ, therefore their local helicities are of opposite sign. Figure 12(*c*) shows isosurfaces of axial vorticity at higher $\xi = \pm 4000$, illustrating that the two vortices are of different strengths. The strongest vortex is the light grey (yellow online) isosurface, corresponding to negative ξ, and therefore the total helicity of this solution is negative, corresponding to a clockwise precession of the thermal plume, as can be seen in the online movie 5.

5.1. *Bifurcations of the precessing plume*

By further increasing the Grashof number, the rotating wave undergoes a sequence of bifurcations to more complicated time-dependent states, as shown in figure 9. The first bifurcation results in a quasi-periodic state (termed MRW in figure 9) illustrated in figure 13, showing temperature contours in the inertial frame (figure 13*a*) and in the frame precessing with the plume (figure 13*b*). In the precessing frame, the plume is periodic, and the new periodicity corresponds to a puff of hot fluid propagating upwards along the tilted plume. The puffing frequency ω_{pu} is easily computed from the time series of the kinetic energy of MRW. Since the kinetic energy is a global

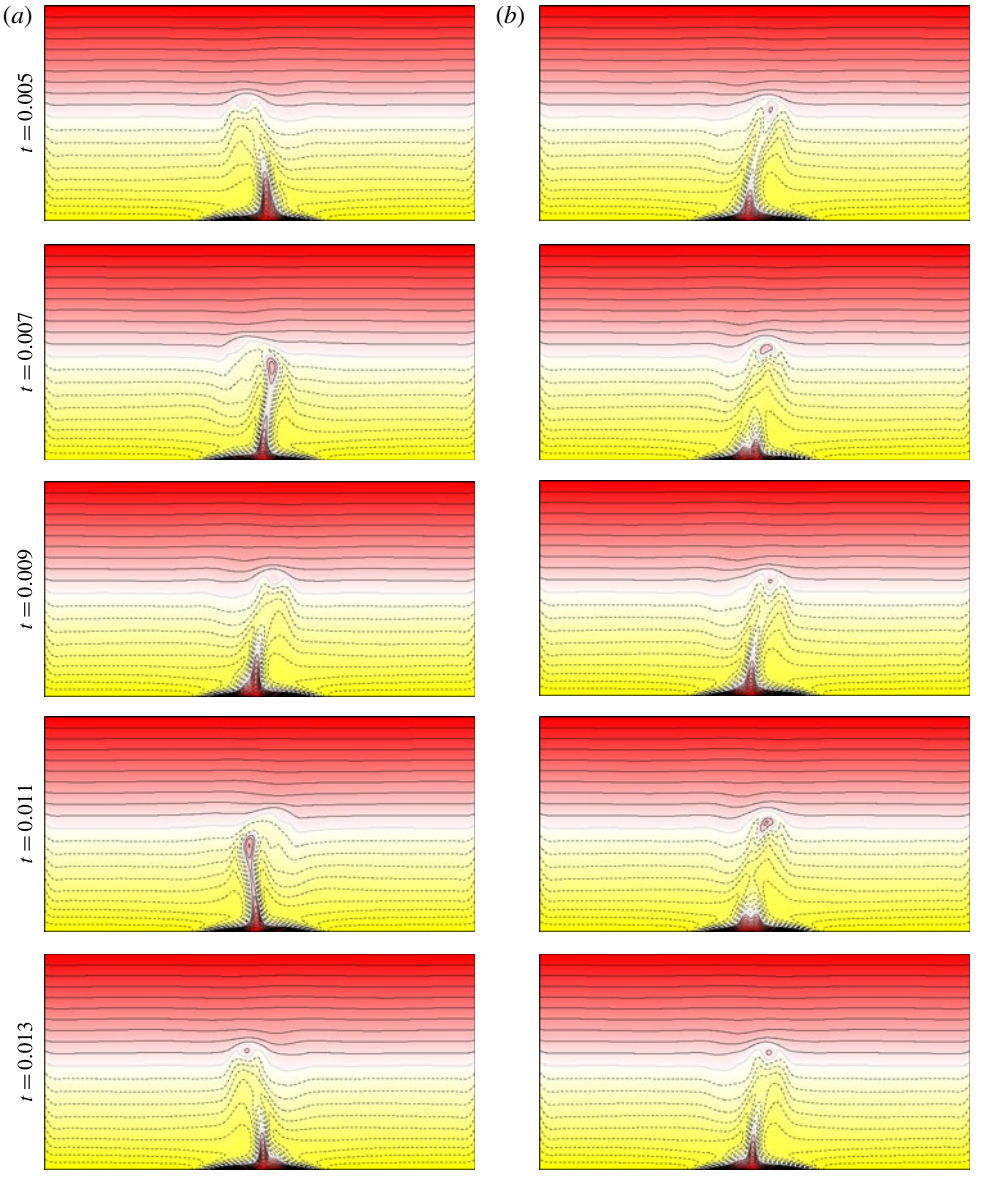

FIGURE 13. (Colour online) Isotherms of MRW at $Gr = 2.5 \times 10^5$ in the inertial (stationary) frame (*a*) and a precessing frame (*b*) with frequency $\omega_{pr} = 7435.0$. There are 10 contour levels with $T \in [-0.5, 0.5]$; solid lines (red) are positive and dashed lines (yellow) are negative.

measure, the precession frequency disappears from its time series and the energies are purely periodic (see figure 15 below). The result is $\omega_{pu} = 1.414 \times 10^4$, which is very close to, but not exactly equal to, twice the precession frequency ($2\omega_{pr} = 1.487 \times 10^4$). The two frequencies can be observed in figure 14, which shows time series of the temperature at three different points in the inertial frame: T_m at the centre of the cell $(r, \theta, z) = (0, 0, 0.5\gamma)$, and T_1 and T_2 at $(r, \theta, z) = (0.1, 0, 0.5\gamma)$ and $(0.1, 0, 0.05\gamma)$, close to the axis and near the top and the base of the plume, respectively. The time

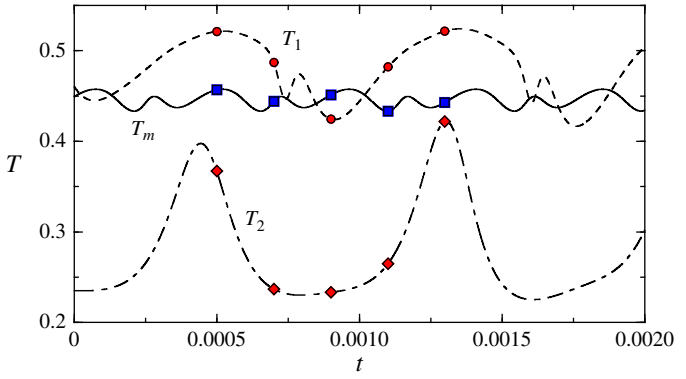

FIGURE 14. (Colour online) Time series of the temperature at various points (r, θ, z): $T_1 = T(0.1, 0, 0.5\gamma)$ (dashed line with circles), $T_m = T(0, 0, 0.5\gamma)$ (solid line with squares), and $T_2 = T(0.1, 0, 0.05\gamma)$ (dot-dashed line with diamonds); the symbols correspond to the isotherm plots shown in figure 13.

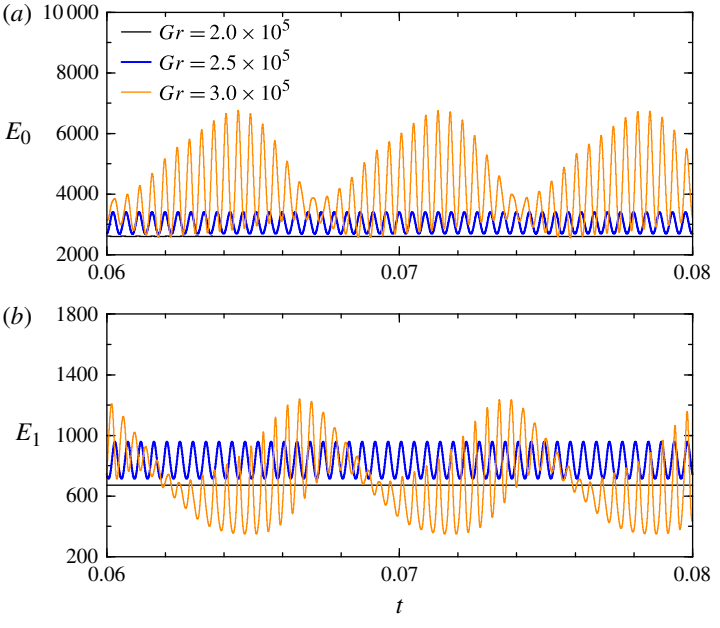

FIGURE 15. (Colour online) Time series of E_0 (a) and E_1 (b) for the states RW, MRW and VLF.

series of T_m is periodic with the period of the puffing $\tau_{pu} = 2\pi/\omega_{pu}$ because the cylinder axis does not precess. The time series of T_1 and T_2 show a periodicity of $\tau_{pr} = 2\pi/\omega_{pr} \approx 2\tau_{pu}$, the precession period, but the periodicity is only approximate because ω_{pu} and ω_{pr} are not in a rational ratio. As a result, the successive peaks are not of the same size and the time series is quasi-periodic. The precessing and puffing plume, MRW, lies on a two-torus and is a modulated rotating wave state.

The puffing phenomenon in MRW is closely related to the puffing we have observed when the computations are restricted to the axisymmetric subspace. In fact,

the precessing and puffing plume at $Gr = 2.5 \times 10^5$, described in figures 13 and 14, has a puffing frequency of $\omega_{pu} = 1.414 \times 10^4$ that lies on the extension of the curve of the axisymmetric puffing ω_0 in figure 8(*a*). This strongly suggests that the two puffing mechanisms, in the axisymmetric subspace and in the full three-dimensional space, are the same. The axisymmetric puffing appears at $Gr \approx 2.84 \times 10^5$, while the puffing plume MRW appears at $Gr \approx 2.35 \times 10^5$. This fact, together with the proximity between ω_{pu} and $2\omega_{pr}$, suggests that the axisymmetric puffing mechanism is excited by the precessing plume before, but close to, it becoming unstable in the axisymmetric subspace, in an approximate 1:2 resonance between the puffing and the precessing frequencies.

On further increasing the Grashof number, the quasi-periodic state MRW develops an additional very low frequency at approximately $Gr \approx 2.8 \times 10^5$ (see figure 9). This new very low-frequency state VLF is clearly apparent in figure 15, showing time series of E_0 and E_1 for the states RW and MRW that have already been described, and the new VLF state at $Gr = 3 \times 10^5$. At this particular Gr, the new frequency is approximately sixteen times smaller than the puffing frequency. Notice that the precession frequency does not appear in the energy time series because it is a global measure (integrating over the whole domain), and therefore the precession does not change the energy values. This VLF state, having three incommensurate frequencies, lies on a three-torus. It is well-known (Ruelle & Takens 1971; Newhouse, Ruelle & Takens 1978) that three frequencies usually means chaos. However, this is not the case here because of the symmetries of the problem. One of the frequencies, the precession frequency ω_{pr}, is associated with the rotational invariance of the cylindrical container and can be removed by changing to a reference frame rotating with ω_{pr}, where the VLF state becomes a two-torus. In fact stable three-tori states have been observed in other hydrodynamics problems with rotational invariance (Lopez & Marques 2000; Marques, Lopez & Shen 2001; Marques, Lopez & Iranzo 2002; Lopez & Marques 2003; Marques & Lopez 2006; Lopez 2006; Avila *et al.* 2007; Lopez & Marques 2009; Altmeyer *et al.* 2012).

The VLF state, as is apparent from figure 15, alternates between a state very similar to the precessing puffing plume MRW (near the minima of E_0), and another state where the axisymmetric component measured by E_0 is substantially stronger, while the non-axisymmetric energy is smaller that that of MRW (near the maxima of E_0), i.e. they resemble axisymmetric puffing states. In fact, the axisymmetric puffing state becomes stable (in the axisymmetric subspace) at about the same value of Gr at which the VLF state appears. This suggests that the VLF state is close to a heteroclinic cycle alternately visiting the MRW solution (now unstable) and the axisymmetric puffing state (stable in the axisymmetric subspace, but unstable to three-dimensional perturbations; the state denoted BS_u in figure 9). The bifurcation giving rise to the VLF state would then be associated with the bifurcation producing the axisymmetric puffing state; it is a global bifurcation of heteroclinic type.

Figure 16 shows four snapshots from a movie of the VLF state, showing the precession of the plume and the puffing process. In figure 16(*a*) the flow is close to axisymmetric, and the tilting of the plume is difficult to see; in figure 16(*d*), the tilting is more apparent, illustrating the VLF excursions between the axisymmetric puffing state and the non-axisymmetric puffing state MRW.

On further increasing the Grashof number, the dynamics becomes more complicated; we have observed a period doubling of the VLF state (the state denoted VLF_{pd} in figure 9) and regions of coexistence of the VLF and MRW states, before the flow becomes temporally chaotic. These additional states have been included in figure 9 up to $Gr = 4 \times 10^5$, but we have not pursued further analysis of these complex states.

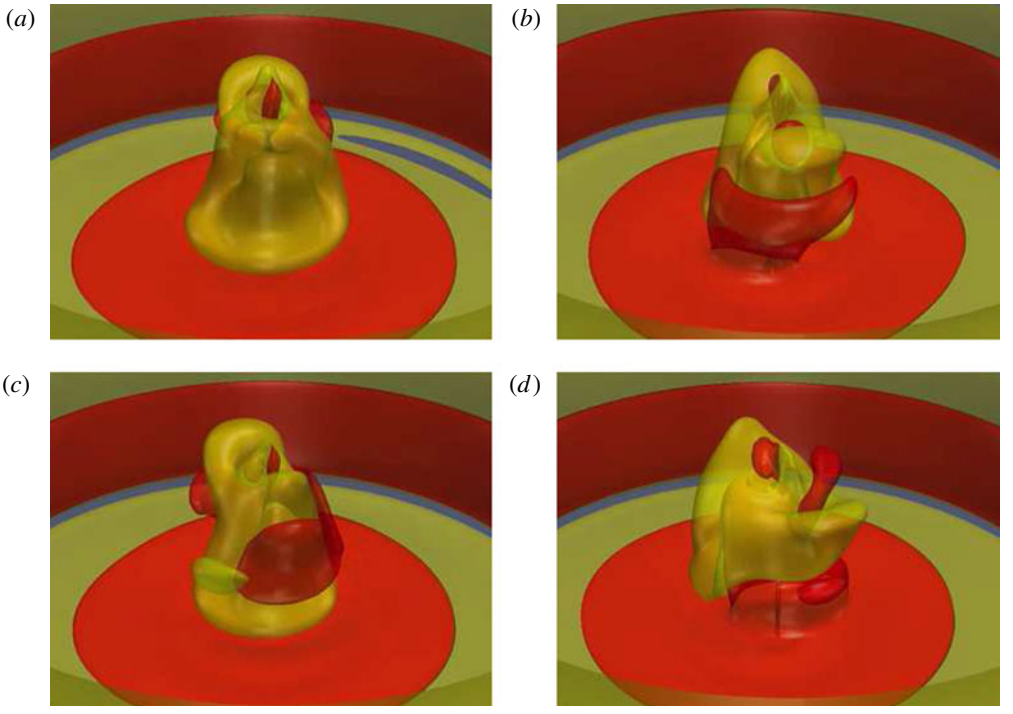

FIGURE 16. (Colour online) Three-dimensional isosurfaces of azimuthal vorticity η, at four equispaced times relative to the online movie, of the VLF state at $Gr = 3.5 \times 10^5, A_r = 2, A_z = 2, A_T = 1$ and $\sigma = 7$. The isosurface levels are at $\eta = \pm 10^3$. See associated online movie.

6. Discussion and conclusions

This study was motivated by the long-standing puzzle that for many plumes, including some geophysical plumes, swirl is sometimes observed, and yet there is not a generally accepted explanation of where it comes from, particularly for plumes whose scales are such that the Coriolis force is not expected to be a primary factor. For the most part, explanations rely on the focusing and amplification of background rotation or shear near the ground by the updraft from the plume. The important issue is to determine if the swirl arises due to extraneous effects (ambient rotation or ambient shear) or due to intrinsic effects. The only way to determine this is to eliminate external disturbances, and this is done by employing an enclosed geometry. The laboratory experiments of Torrance (1979) considered a plume in a completely enclosed cylinder driven by a localized hot spot on the bottom boundary. In a parameter regime where the ambient stratification is not too weak or too strong, the onset of swirl in a plume was observed, but no details of the flow nor any explanation of what the swirl was due to were offered. Nevertheless, the completely enclosed experiments suggest that the onset of swirl could be intrinsic to the plume dynamics.

In order to investigate this idea, we have simulated the flow in a stationary fully enclosed cylinder driven by a localized hot spot at the bottom, in a stratified ambient that is maintained by a linearly decreasing fixed temperature up the sidewall. We fix the ratio of the temperature difference between the top and bottom of the sidewall to the temperature difference between the centre of the hot spot and the bottom of the

side to be $A_T = 1$ (this results in the plume's neutral buoyancy level being at about the cylinder half-height), as well as fixing the geometry and fluid (water), and we explore the dynamics of the plume as the Grashof number Gr is increased. Increasing the Grashof number corresponds to increasing the temperature of the centre of the hot spot relative to the temperature of the bottom of the sidewall, and since $A_T = 1$ this also means that the buoyancy frequency of the ambient stratification is increased proportionally with $\sqrt{Gr}$.

When the simulations are restricted to being axisymmetric, the steady plume flow loses stability to a puffing mode via a Hopf bifurcation at $Gr \approx 2.84 \times 10^5$. The features of the puffing mode are very similar to those of the puffing mode in an isothermal ambient (Lopez & Marques 2013), with the one notable difference being that the plume in the stratified ambient does not penetrate all the way to the ceiling. In both the isothermal ambient and the present stratified ambient cases, the steady axisymmetric plume state loses stability to three-dimensional disturbances at Gr significantly lower than the critical Gr for the axisymmetric puffing mode instability. However, the manner in which axisymmetry is broken in the two cases is very different. They both break the invariance to rotations, R_α, but while the plume in an isothermal ambient preserves parity, K_β, parity is broken in the stratified ambient case. It is this parity-breaking Hopf bifurcation which results in the swirling plume. Near onset ($Gr \gtrsim 1.18 \times 10^5$), the swirling plume is a rotating wave possessing non-zero mean helicity, and its precession frequency is approximately $1/\sqrt{2}$ times the buoyancy frequency, and so internal waves are emitted at approximately 45°. On further increasing $Gr > 2.4 \times 10^5$, the swirling plume is modulated. The modulation is due to a puff of hot fluid propagating upwards along the tilted swirling plume. We find that the precession frequency is exciting the puffing mode subharmonically at Gr values a little below where the puffing mode sets in in the absence of the swirl; the precession frequency is about half the puffing frequency. As Gr is increased beyond approximately 2.8×10^5, the plume is further modulated by a very low frequency. We show that this results from a global bifurcation and this very low-frequency modulated plume is close to a heteroclinic cycle where the flow slowly drifts from a state resembling the axisymmetric puffing mode to a state resembling the rotating wave swirling plume. In summary, swirl results spontaneously from an intrinsic instability breaking parity symmetry. Subsequent instabilities lead to quite complicated spatio-temporal behaviour. These results provides a new perspective with which to re-visit the question of how do naturally occurring plumes, such as dust devils, acquire their swirl.

Acknowledgements

This work was supported by the National Science Foundation grants DMS-0922864 and CBET-1336410, and the Spanish Ministry of Education and Science grant (with FEDER funds) FIS2013-40880.

Supplementary movies

Supplementary movies are available at http://dx.doi.org/10.1017/jfm.2014.628.

REFERENCES

ALTMEYER, S., DO, Y., MARQUES, F. & LOPEZ, J. M. 2012 Symmetry-breaking Hopf bifurcations to 1-, 2-, and 3-tori in small-aspect-ratio counterrotating Taylor–Couette flow. *Phys. Rev.* E **86**, 046316.

AVILA, M., MARQUES, F., LOPEZ, J. M. & MESEGUER, A. 2007 Stability control and catastrophic transition in a forced Taylor–Couette system. *J. Fluid Mech.* **590**, 471–496.

BATTAGLIA, F., REHM, R. G. & BAUM, H. R. 2000 The fluid mechanics of fire whirls: an inviscid model. *Phys. Fluids* **12**, 2859–2867.

BUSSE, F. H. 1967 The stability of finite amplitude cellular convection and its relation to an extremum principle. *J. Fluid Mech.* **30**, 625–649.

CARROLL, J. J. & RYAN, J. A. 1970 Atmospheric vorticity and dust devil rotation. *J. Geophys. Res.* **75**, 5179–5184.

CHOSSAT, P. & LAUTERBACH, R. 2000 *Methods in Equivariant Bifurcations and Dynamical Systems*. World Scientific.

CORTESE, T. & BALACHANDAR, S. 1993 Vortical nature of thermal plumes in turbulent convection. *Phys. Fluids* A **5**, 3226–3232.

CRAWFORD, J. D. & KNOBLOCH, E. 1991 Symmetry and symmetry-breaking bifurcations in fluid dynamics. *Annu. Rev. Fluid Mech.* **23**, 341–387.

EMMONS, H. W. & YING, S.-J. 1967 The fire whirl. In *Proceedings 11th International Symposium on Combustion*, pp. 475–488. Combustion Institute.

FIEDLER, B. H. & KANAK, K. M. 2001 Rayleigh-Bénard convection as a tool for studying dust devils. *Atmos. Sci. Lett.*; doi:10.1006/asle.2001.0043.

GRAY, D. D. & GIORGINI, A. 1976 The validity of the Boussinesq approximation for liquids and gases. *Intl J. Heat Mass Transfer* **19**, 545–551.

KNOBLOCH, E. 1996 Symmetry and instability in rotating hydrodynamic and magnetohydrodynamic flows. *Phys. Fluids* **8**, 1446–1454.

KUZNETSOV, Y. A. 2004 *Elements of Applied Bifurcation Theory*, 3rd edn. Springer.

LOPEZ, J. M. 2006 Rotating and modulated rotating waves in transitions of an enclosed swirling flow. *J. Fluid Mech.* **553**, 323–346.

LOPEZ, J. M. & MARQUES, F. 2000 Dynamics of 3-tori in a periodically forced Navier–Stokes flow. *Phys. Rev. Lett.* **85**, 972–975.

LOPEZ, J. M. & MARQUES, F. 2003 Small aspect ratio Taylor–Couette flow: onset of a very-low-frequency three-torus state. *Phys. Rev.* E **68**, 036302.

LOPEZ, J. M. & MARQUES, F. 2009 Centrifugal effects in rotating convection: nonlinear dynamics. *J. Fluid Mech.* **628**, 269–297.

LOPEZ, J. M. & MARQUES, F. 2013 Instability of plumes driven by localized heating. *J. Fluid Mech.* **736**, 616–640.

MARQUES, F. & LOPEZ, J. M. 2006 Onset of three-dimensional unsteady states in small aspect-ratio Taylor–Couette flow. *J. Fluid Mech.* **561**, 255–277.

MARQUES, F., LOPEZ, J. M. & IRANZO, V. 2002 Imperfect gluing bifurcation in a temporal glide-reflection symmetric Taylor–Couette flow. *Phys. Fluids* **14**, L33–L36.

MARQUES, F., LOPEZ, J. M. & SHEN, J. 2001 A periodically forced flow displaying symmetry breaking via a three-tori gluing bifurcation and two-tori resonances. *Physica* D **156**, 81–97.

MASSAGUER, J. M. & MERCADER, I. 1988 Instability of swirl in low-Prandtl number thermal convection. *J. Fluid Mech.* **189**, 367–395.

MASSAGUER, J. M., MERCADER, I. & NET, M. 1990 Nonlinear dynamics of vertical vorticity in low-Prandtl number thermal convection. *J. Fluid Mech.* **214**, 579–597.

MAXWORTHY, T. 1973 A vorticity source for large-scale dust devils and other comments on naturally occurring columnar vortices. *J. Atmos. Sci.* **30**, 1717–1722.

MERCADER, I., BATISTE, O. & ALONSO, A. 2010 An efficient spectral code for incompressible flows in cylindrical geometries. *Comput. Fluids* **39**, 215–224.

MORTON, B. R. 1966 Geophysical vortices. *Prog. Aerosp. Sci.* **7**, 145–194.

MORTON, B. R., TAYLOR, G. & TURNER, J. S. 1956 Turbulent gravitational convection from maintained and instantaneous sources. *Proc. R. Soc. Lond.* A **234**, 1–23.

MUNROE, J. R. & SUTHERLAND, B. R. 2014 Internal wave energy radiated from a turbulent mixed layer. *Phys. Fluids* **26**, 096604.

MURASZEW, A., FEDELE, J. B. & KUBY, W. C. 1979 The fire whirl phenomenon. *Combust. Flame* **34**, 29–45.

MURPHY, J. O. & LOPEZ, J. M. 1984 The influence of vertical vorticity on thermal convection. *Austral J. Phys.* **37**, 41–62.

NEWHOUSE, S., RUELLE, D. & TAKENS, F. 1978 Occurrence of strange axiom-A attractors near quasi-periodic flows on T^m, $m \geqslant 3$. *Commun. Math. Phys.* **64**, 35–40.

RUELLE, D. & TAKENS, F. 1971 On the nature of turbulence. *Commun. Math. Phys.* **20**, 167–192.

SNOW, J. T. 1987 Atmospheric columnar vortices. *Rev. Geophys.* **25**, 371–385.

SPEER, K. G. & MARSHALL, J. 1995 The growth of covective plumes at seafloor hot springs. *J. Mar. Res.* **53**, 1025–1057.

STROGATZ, S. 1994 *Nonlinear Dynamics and Chaos*. Addison-Wesley.

SUTHERLAND, B. R. & LINDEN, P. F. 1998 Internal wave excitation from stratified flow over a thin barrier. *J. Fluid Mech.* **377**, 223–252.

TORRANCE, K. E. 1979 Natural convection in thermally stratified enclosures with localized heating from below. *J. Fluid Mech.* **95**, 477–495.

TORRANCE, K. E., ORLOFF, L. & ROCKETT, J. A. 1969 Experiments on natural convection in enclosures with localized heating from below. *J. Fluid Mech.* **36**, 21–31.

TORRANCE, K. E. & ROCKETT, J. A. 1969 Numerical study of natural convection in an enclosure with localized heating from below – creeping flow to the onset of laminar instability. *J. Fluid Mech.* **36**, 33–54.

WOODS, A. W. 2010 Turbulent plumes in nature. *Annu. Rev. Fluid Mech.* **42**, 391–412.